Perturbed angular distribution of electrons following photoionization of $6sns\ ^1S_0$ barium Rydberg states

H. Hieronymus, M. Kohl,* J. Neukammer,* A. König, and H. Rinneberg*
Institut für Atom- und Festkörperphysik, Freie Universität Berlin, Arnimallee 14, 1000 Berlin 33, West Germany

H. Spinger-Bolk
Coherent G.m.b.H., Senefelderstrasse 10, 6074 Rödermark, West Germany
(Received 31 July 1989)

Combining high-resolution laser and electron spectroscopy, we have measured angular distributions of electrons emitted from autoionizing Rydberg states close to the $6p\ ^2P_{1/2}$ and $6p\ ^2P_{3/2}$ ionization limits of barium. Starting from $6sns\ ^1S_0$ ($12 \le n \le 100$) Rydberg levels, $[6p_{1/2}n's]_{J=1}$ ($24 \le n' \le 50$), $[6p_{1/2}n'd]_{J=1}$ ($22 \le n' \le 49$), and $[6p_{3/2}ns]_{J=1}$ and $[6p_{3/2}n'd]_{J=1}$ ($11 \le n' \le 99$) autoionizing Rydberg states were reached by exciting their $6p_{3/2}ns$ components. Alternatively, by inducing the transition $6s \rightarrow 6p_{1/2}$ of the (Ba^+) ionic core, the $[6p_{1/2}24s]_{J=1}$ and the neighboring $[6p_{1/2}22d]_{J=1}$ and $[6p_{1/2}23d]_{J=1}$ states were excited starting from the $6s24s\ ^1S_0$ Rydberg level. We have observed pronounced resonances in the asymmetry parameters β corresponding to the final ionic states $Ba^+\ 6s\ ^2S_{1/2}$, $5d\ ^2D_{3/2}$, and $5d\ ^2D_{5/2}$. These resonances appear in the vicinity of the $[6p_{1/2}n's]_{J=1}$, $[6p_{1/2}n'd]_{J=1}$, and $[6p_{3/2}n'd]_{J=1}$ autoionizing Rydberg states and are caused by configuration interaction with the $[6p_{3/2}ns]_{J=1}$ Rydberg series. Above the $6p\ ^2P_{1/2}$ ionization limit the shape of the β resonances was found to be independent of the principal quantum number. In contrast, the β resonances associated with $[6p_{1/2}n's]_{J=1}$ and $[6p_{1/2}n'd]_{J=1}$ autoionizing Rydberg states change their shapes within the contour of the $[6p_{3/2}12s]_{J=1}$ perturbing state. In addition to angular distributions we have measured the yield of electrons, leaving the ion in its ground state as well as the total ion yield by scanning the (third) laser across the $[6p_{3/2}12s]_{J=1}$ perturbing resonance. In addition, kinetic energies of emitted electrons were measured at fixed total excitation energies falling within the contour of the perturbing resonance. Total ion yields, partial ion yields, and electron yields corresponding to the Ba^+ ground state as well as branching ratios to the $^2S_{1/2}$, $^2D_{3/2}$, and $^2D_{5/2}$ final ionic states exhibit pronounced resonances which have been correlated with the resonances observed in the asymmetry parameters. For each final ionic state a simple multichannel quantum defect model was used to calculate the asymmetry parameter β as a function of excitation energy. Good agreement with asymmetry parameters derived from experiment was achieved.

I. INTRODUCTION

Ground-state photoionization has played a major role in elucidating the structure of complex atoms.[1] The interplay between direct photoionization on one hand and the excitation of autoionizing states and their subsequent decay on the other hand results in the well-known Fano-Beutler profiles. For Rydberg states, however, photoionization of the outer electron can be neglected and hence photoionization proceeds exclusively via excitation and decay of autoionizing resonances. Within the last decade, photoionization of Rydberg states of alkaline-earth atoms has been investigated both experimentally[2-17] and theoretically.[4-21] Starting from bound Rydberg states of alkaline-earth atoms, autoionizing resonances are easily reached by resonant excitation of the inner valence electron, i.e., by isolated core excitation.[3] Employing this technique, photoionization cross sections, branching ratios, and angular distributions of photoelectrons have been measured. Configuration interactions of autoionizing Rydberg series considerably complicate the physical situation. For example, the $[6p_{3/2}12s]_{J=1}$ autoionizing state of barium is degenerate with a large number of $[6p_{1/2}ns]_{J=1}$ and $[6p_{1/2}nd_{3/2}]_{J=1}$ Rydberg states, which cause additional resonances in the broad contour of the $[6p_{3/2}12s]_{J=1}$ resonance.[4] In addition, configuration interactions are responsible for resonant variations in branching ratios and asymmetry parameters observed as a function of energy.[13,14,17] Multichannel quantum-defect theory (MQDT), which takes configuration interactions into account, has frequently been used to analyze experimental data obtained in photoionization studies of Rydberg states of alkaline-earth atoms. Recently eigenchannel R-matrix calculations have been successfully performed for Ca (Refs. 19 and 20) and Sr (Ref. 21). The results have been compared with experimental densities of oscillator strengths, branching ratios, and asymmetry parameters.

In this contribution we report photoionization studies of $6sns\ ^1S_0$ Rydberg states of barium with principal quantum numbers up to $n = 100$. In particular, we have studied the influence of configuration interactions between the $[6p_{1/2}ns]_{J=1}$ and $[6p_{1/2}nd_{3/2}]_{J=1}$ Rydberg series and the $[6p_{3/2}12s]_{J=1}$ perturbing state on the electron

angular distributions as well as branching ratios. The asymmetry parameters and branching ratios have been determined as a function of excitation energy and numerous resonances as well as changes in their line shapes have been observed. In addition, resonances in the asymmetry parameters have been detected in the vicinity of $[6p_{3/2}nd]_{J=1}$ autoionizing states above the $6p\ ^2P_{1/2}$ threshold. The appearance of the latter resonances is being interpreted as clear evidence for configuration interaction between the $[6p_{3/2}ns]_{J=1}$ and $[6p_{3/2}nd]_{J=1}$ Rydberg series. This is consistent with previous explanations of the resonant variation of branching ratios in the vicinity of the $[6p_{3/2}nd]_{J=1}$ states.[14] Our experiments extend recent investigations of the angular distributions of electrons, following photoionization of $6sns\ ^1S_0$ barium Rydberg states.[6,9,11] Previously the angular distribution of electrons was measured at discrete excitation energies corresponding to the center of the $[6p_{1/2}ns]_{J=1}$ and $[6p_{3/2}ns]_{J=1}$ $(n \leq 25)$ autoionizing Rydberg states, employing pulsed dye laser excitation. On the contrary, the use of cw dye lasers has allowed us to use an electron spectrometer with excellent angular and energy resolution. Because of the high count rates achieved we were able to measure angular distributions of electrons as a function of excitation energy with high precision. In this way more detailed experimental information has been obtained than in previous studies of angular distributions of electrons emitted from autoionizing Rydberg states of alkaline-earth atoms.

II. EXPERIMENT

We have employed different three-step excitation schemes to reach odd parity, $J=1$ autoionizing Rydberg states of barium converging towards the $6p\ ^2P_{1/2}$ and $6p\ ^2P_{3/2}$ ionization limits, respectively. Starting from the atomic ground state $6s^2\ ^1S_0$, $6sns\ ^1S_0$ Rydberg states were populated via the $6s6p\ ^1P_1$ intermediate level (Fig. 1). The last step of our excitation scheme corresponds to an isolated core excitation $6sns \rightarrow 6p_{1/2}ns$ [Fig. 1(a)] or $6sns \rightarrow 6p_{3/2}ns$ [Figs. 1(b) and 1(c)]. We have reached $[6p_{1/2}n's]_{J=1}$ $(24 \leq n' \leq 50)$ and $[6p_{1/2}n'd]_{J=1}$ $(22 \leq n' \leq 49)$ Rydberg states, starting from the $6s12s\ ^1S_0$ intermediate level, by exciting their $[6p_{3/2}12s]_{J=1}$ character [Fig. 1(b)]. These autoionizing Rydberg states fall within the broad contour of the $[6p_{3/2}12s]_{J=1}$ perturber and are heavily mixed with it due to configuration interaction. Alternatively, we have populated the $[6p_{1/2}24s]_{J=1}$ and neighboring $[6p_{1/2}22d]_{J=1}$ and $[6p_{1/2}23d]_{J=1}$ Rydberg states starting from the $6s24s\ ^1S_0$ intermediate level by inducing the core transition $6s \rightarrow 6p_{1/2}$ [Fig. 1(a)]. Configuration interaction between $[6p_{1/2}ns]_{J=1}$ and $[6p_{1/2}(n-1)d]_{J=1}$, $[6p_{1/2}(n-2)d]_{J=1}$ Rydberg states enables us to excite the $[6p_{1/2}24s]_{J=1}$ character in each case. In addition, starting from $6sns\ ^1S_0$ $(n \geq 13)$ intermediate levels, $[6p_{3/2}ns]_{J=1}$, $[6p_{3/2}(n-1)d]_{J=1}$, and $[6p_{3/2}(n-2)d]_{J=1}$ autoionizing states were reached by inducing the $6s \rightarrow 6p_{3/2}$ transition of the ionic core, exploiting the configuration interaction between both series. Figure 2 shows the experimental setup which we used to measure angular distributions of electrons. Three cw dye lasers with a bandwidth of about 1 MHz were employed. The first and second dye laser were operated with Rhodamine 110 and Stilbene 3 as laser dyes and stabilized by means of a reference experiment (Fig. 3) to the atomic transitions $6s^2\ ^1S_0 \rightarrow 6s6p\ ^1P_1$ and $6s6p\ ^1P_1 \rightarrow 6sns\ ^1S_0$, respectively. In order to scan the spectral profiles of broad as well as narrow autoionizing resonances, a computer-controlled Ar^+ laser pumped dye laser (Coherent Autoscan) with a tuning range of about 5 THz was used. This

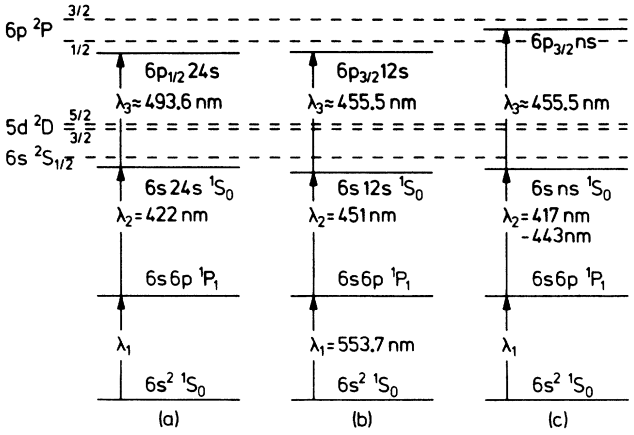

FIG. 1. Three-step excitation schemes for $[6p_j ns, nd]_{J=1}$ autoionizing Rydberg states of barium. The five lowest ionization limits are indicated by dashed lines.

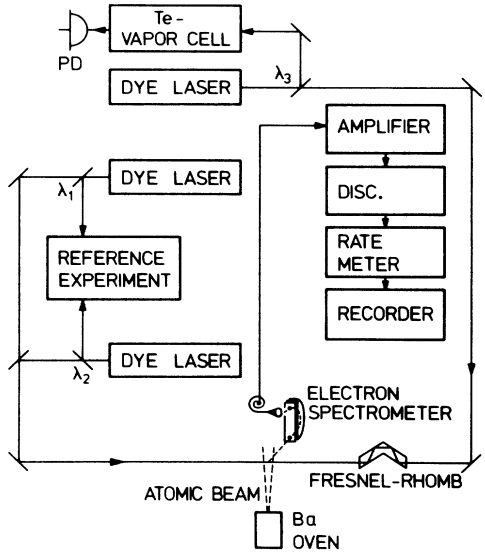

FIG. 2. Experimental setup used to measure electron yields, electron kinetic energies, and angular distributions of emitted electrons. The reference experiment (see Fig. 3) served to actively stabilize two of the three cw dye lasers to the first (λ_1) and second (λ_2) atomic transition, respectively. The abbreviations PD and DISC stand for photodiode and discriminator, respectively.

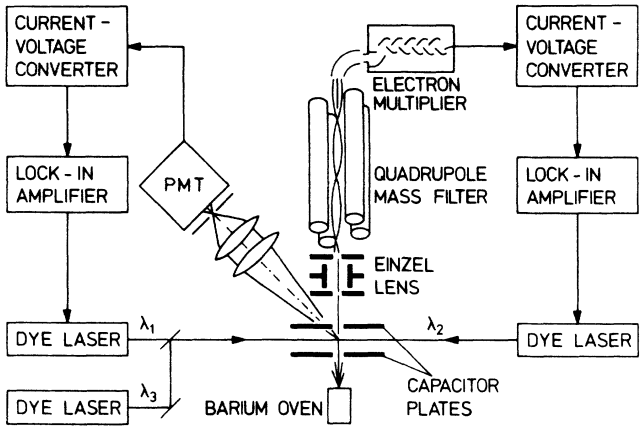

FIG. 3. Experimental setup referred to as "reference experiment" in Fig. 2. The first dye laser (λ_1) was stabilized to the first atomic transition (see Fig. 1) by observing the fluorescence emitted from the $6s6p\ ^1P_1$ intermediate level using a photomultiplier tube (PMT). The second dye laser (λ_2) was stabilized by counting Ba^+ ions produced by collisional ionization of $6sns\ ^1S_0$ ($n \geq 14$) Rydberg states. In addition the experimental setup served to measure total ion yields following ionization by means of the third dye laser (λ_3).

dye laser was operated with Coumarin 6 or Stilbene 3 in order to produce laser radiation with frequencies in the vicinity of the ionic transitions $6s\ ^2S_{1/2} \rightarrow 6p\ ^2P_{1/2}$ and $6s\ ^2S_{1/2} \rightarrow 6p\ ^2P_{3/2}$, respectively. The wavelength of the laser radiations were measured using a Burleigh wavemeter. In addition, the wavelength of the third dye laser (λ_3) was determined by means of the wavemeter incorporated into the Coherent Autoscan dye laser. For absolute determination of the wavelength λ_3 we measured the absorption spectra of $^{130}Te_2$ dimers.[22] All laser beams with a diameter of about 1.5 mm were superimposed and intersected a well-collimated atomic beam of barium perpendicularly. The third laser beam counterpropagated with respect to the laser beams of the first and second dye laser. Typical laser powers used to induce the first, second, and third atomic transition amounted to 20 μW, 50 mW, and 150 mW, respectively. The power densities of the first and second laser beam as well as the number density of the barium atomic beam were kept low enough to avoid Penning ionization of the $6sns\ ^1S_0$ Rydberg states.[23] A lens with a focal length of 160 mm was employed to increase the power density of the third laser beam in the interaction region. The polarization vector of the linearly polarized third laser beam was rotated by means of a Fresnel rhomb. Three mutually perpendicular pairs of Helmholtz coils were used to compensate the earth's magnetic field to about 1%. A scattering chamber shielded the interaction region from stray electric fields. The background pressure was about 10^{-4} Pa. A simulated spherical capacitor spectrometer[24] outside the scattering chamber allowed us to analyze the kinetic energy of electrons emitted perpendicularly to the atomic and laser beams. The full acceptance angle of the spectrometer was about 2°. Electrons were detected by means of a channel electron multiplier and counted using standard electronics. The spectrometer was operated in the constant pass energy mode. Keeping the frequencies of all dye lasers fixed, electron spectra were recorded by scanning the voltage which accelerated electrons emerging from the scattering chamber. Typically an energy resolution of 20 meV full width at half maximum (FWHM) was achieved. Angular distributions of electrons were measured by rotating the Fresnel rhomb (Fig. 2) while keeping the acceleration voltage tuned to an electron kinetic energy corresponding to a selected final ionic state. Figure 4(a) shows the distribution of kinetic energies of electrons emitted from the $[6p_{1/2}29s]_{J=1}$ autoionizing Rydberg state, close to the total excitation energy of 62 117.25 cm^{-1}. The perturbed autoionizing Rydberg state was reached via the $6s12s\ ^1S_0$ state, employing the excitation scheme shown in Fig. 1(b). The polarization vector of the third laser beam coincided with the direction of observation ($\theta = 0°$). Three prominent signals are observed which correspond to the final ionic states Ba^+ $5d\ ^2D_{5/2}$, $5d\ ^2D_{3/2}$, and $6s\ ^2S_{1/2}$. The ^2D fine-structure doublet with an energy splitting of 100 meV only is well resolved. Because of the high electron yields due to the use of cw lasers, count rates up to $10^4\ s^{-1}$ were obtained

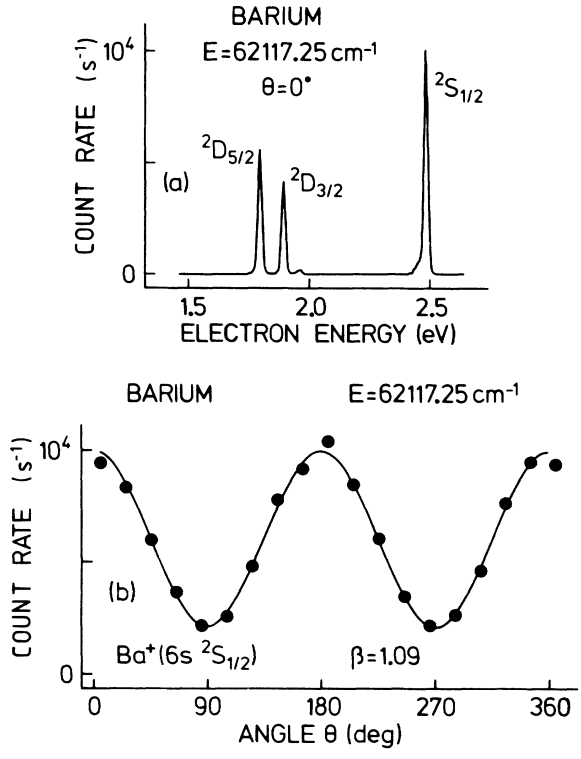

FIG. 4. (a) Electron spectrum and (b) electron angular distribution after excitation of the $[6p_{1/2}29s_{1/2}]_{J=1}$ autoionizing Rydberg state. In (a) the count rate has been plotted vs the kinetic energy of the emitted electrons observed parallel to the polarization direction of the third laser beam ($\theta = 0°$). In (b) the spectrometer was tuned to the kinetic energy of electrons leaving the Ba^+ ions in their ground state $6s\ ^2S_{1/2}$. The angle θ between the polarization vector and the direction of observation was varied by rotating the Fresnel rhomb.

despite the high energy resolution and small acceptance angle of the electron spectrometer. The angular distribution of electrons corresponding to the Ba^+ ($^2S_{1/2}$) signal [Fig. 4(a)] is illustrated in Fig. 4(b). The solid line is a least-squares fit of the expression

$$I(\theta)=(I_0/4\pi)[1+\beta P_2(\cos\theta)] \quad (1)$$

to the experimentally observed count rates. The asymmetry parameters $\beta_{1/2}$, $\beta_{3/2}$, and $\beta_{5/2}$ corresponding to the final ionic states $6s\,^2S_{1/2}$, $5d\,^2D_{3/2}$, and $5d\,^2D_{5/2}$ were obtained as a function of excitation energy above and below the $6p\,^2P_{1/2}$ threshold. Electrons associated with the $6p\,^2P_{1/2}$ final ionic state could not be detected in our experimental setup because of their low kinetic energies.

The reference experiment (Fig. 3) served to monitor the excitation of the $6s6p\,^1P_1$ and $6sns\,^1S_0$ intermediate levels and to actively stabilize the frequencies of the first and second dye laser. For this purpose we have imaged the fluorescence of the $6s6p\,^1P_1$ intermediate level onto the photocathode of a photomultiplier. The photomultiplier output signal was fed into a lock-in amplifier, the output of which was applied to the external scan control of a Spectra Physics Model 380 D single-mode dye laser, locking this laser to the $6s^2\,^1S_0 \rightarrow 6s6p\,^1P_1$ atomic transition. The population of $6sns\,^1S_0$ Rydberg states ($n>13$) was monitored by counting Ba^+ ions, produced by collisional and field ionization.[25] Low-lying $6sns\,^1S_0$ ($n=12,13$) Rydberg states were photoionized by means of the third dye laser. The Ba^+ ions produced were focused onto the entrance aperture of a quadrupole mass filter and detected by a secondary electron multiplier. Its output signal was used to lock the second dye laser to the $6s6p\,^1P_1 \rightarrow 6sns\,^1S_0$ transition in the same way as described above.

In Fig. 5 we compare variations in the asymmetry parameter $\beta_{1/2}$ [Fig. 5(a)] with resonances in the partial [Fig. 5(b)] and total photoionization cross sections [Fig. 5(c)]. The resonances appear in the vicinity of $[6p_{1/2}ns]_{J=1}$ and $[6p_{1/2}nd]_{J=1}$ Rydberg states and are caused by configuration interaction of these series with the broad ($\Gamma\approx 85$ cm^{-1}) $[6p_{3/2}12s]_{J=1}$ perturber centered at $E\approx 62\,150$ cm^{-1}. Starting from the $6s12s\,^1S_0$ Rydberg state the angular distribution of the emitted electrons was measured at discrete excitation energies, using the experimental setup illustrated in Fig. 2. On the other hand, the spectrum shown in Fig. 5(b) was recorded by scanning the frequency of the third laser and detecting electrons, emitted along the polarization vector of the third laser beam. The voltage of the electron spectrometer was tuned to the $6s\,^2S_{1/2}$ final ionic state and had to be readjusted after an increase in the laser frequency by about 2 THz, corresponding to 8 meV. The total ion yield [Fig. 5(c)] was measured employing the experimental setup shown in Fig. 3.

The prominent symmetric resonances in the asymmetry parameter $\beta_{1/2}$, associated with $[6p_{1/2}ns]_{J=1}$ Rydberg states correlate with narrow window resonances in the partial cross section and total ion yield. On the contrary, $[6p_{1/2}nd_{3/2}]_{J=1}$ states cause broad window resonances in the cross sections and minor dispersion-like

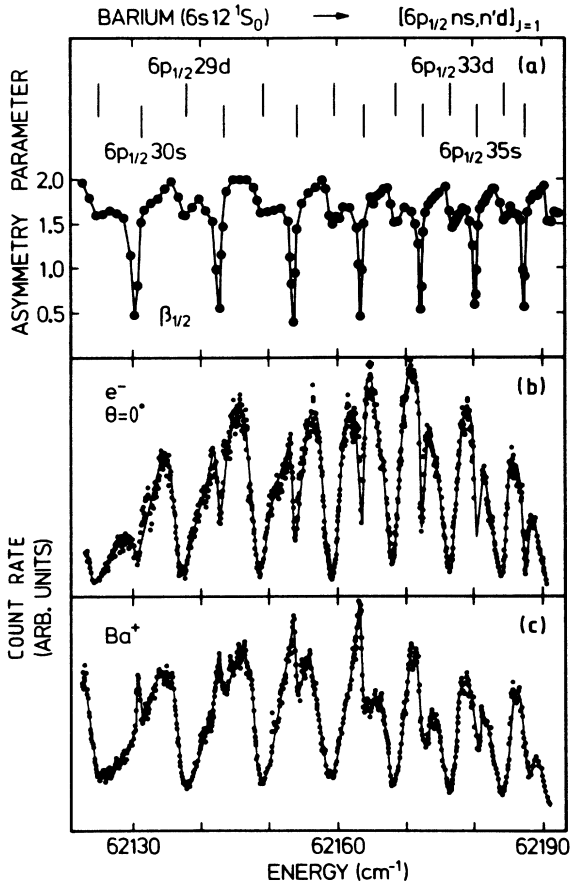

FIG. 5. Comparison of (a) asymmetry parameters, (b) electron yields, and (c) total ion yields close to the center of the $[6p_{3/2}12s]_{J=1}$ autoionizing resonance. Prominent and minor resonances in the (a) asymmetry parameters as well as (b) narrow and broad variations in the electron and (c) ion yields are caused by autoionizing Rydberg states $[6p_{1/2}ns]_{J=1}$ and $[6p_{1/2}nd_{3/2}]_{J=1}$, marked in the upper part of this figure. Dots representing experimental data have been connected to guide the eye. The upper and second trace correspond to the final ionic state Ba^+ $6s\,^2S_{1/2}$. In (b) the electrons were observed along the polarization direction of the third laser beam ($\theta=0°$).

variations in the asymmetry parameter $\beta_{1/2}$. A detailed discussion of these resonances as well as those observed for the $5d\,^2D_{3/2}$ and $^2D_{5/2}$ final ionic states will be given in Sec. IV.

III. THEORETICAL BACKGROUND

The transferred angular momentum formalism, developed by Fano and Dill[26] will be used to analyze measured photoionization cross sections and experimentally obtained asymmetry parameters quantitatively. In this section we briefly summarize the pertinent expressions closely following the presentation of the formalism given by Dill.[27]

The photoionization of $6sns\,^1S_0$ Rydberg states of barium is represented by the following reaction:

$$Ba(J_0=0,\pi_0=+1)+\gamma(j_\gamma=1,\pi_\gamma=-1)$$
$$\rightarrow Ba^+(J_c,\pi_c)+e^-(s=\tfrac{1}{2},l,j,\pi_e=(-1)^l)\ . \quad (2)$$

Here J_0 and π_0 are the total angular momentum and parity quantum numbers of the $6sns\ ^1S_0$ Rydberg states, and j_γ and π_γ refer to the incoming photon γ. The angular momentum quantum numbers of the final ionic states (J_c) and outgoing electrons (l,j) are given in Fig. 6, which illustrates all final ionic states and open channels relevant in the energy range under consideration. Conservation of angular momentum ($\mathbf{J}_0+\mathbf{j}_\gamma=\mathbf{J}_c+\mathbf{s}+\mathbf{l}$) and parity ($\pi_0\pi_\gamma=\pi_c\pi_e$) restricts the possible values of the angular momentum $\mathbf{j}_t$, transferred in the photoionization process

$$\mathbf{j}_t\equiv\mathbf{J}_c+\mathbf{s}-\mathbf{J}_0=\mathbf{j}_\gamma-\mathbf{l}\ . \quad (3)$$

Photoionization processes for which $\pi_0\pi_c=(-1)^{j_t}$ are called parity favored, while $\pi_0\pi_c=(-1)^{j_t+1}$ applies to parity unfavored processes. The asymmetry parameter β describing the angular dependence of the differential photoionization cross section

$$\frac{d\sigma}{d\Omega}=[\sigma(J_c)/4\pi][1+\beta_{J_c}P_2(\cos\theta)] \quad (4)$$

is given as a sum over all parity favored and parity unfavored transitions.[27] The asymmetry parameter is expressed in terms of photoionization amplitudes $S_l(j_t)$, characterized by quantum numbers of the transferred angular momentum $\mathbf{j}_t$ and the orbital angular momentum of the outgoing electron. From the general expressions given in Ref. 27 we derive the following formulas for the asymmetry parameters $\beta_{1/2}$, $\beta_{3/2}$, and $\beta_{5/2}$, associated with the $^2S_{1/2}$, $^2D_{3/2}$, and $^2D_{5/2}$ final ionic states:

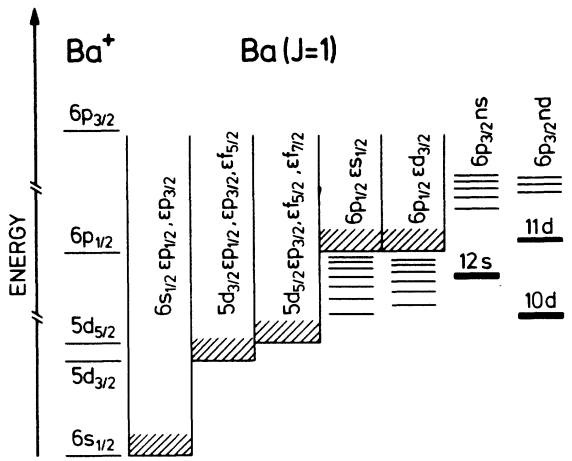

FIG. 6. Open and closed odd-parity $J=1$ channels. The $[6p_{3/2}nd]_{J=1}$ channel comprises the $nd_{3/2}$ and $nd_{5/2}$ fine-structure components. The $[6p_{3/2}12s]_{J=1}$ and $[6p_{3/2}10d]_{J=1}$ autoionizing states are degenerate with a large number of $[6p_{1/2}ns,nd_{3/2}]_{J=1}$ autoionizing Rydberg states. The five lowest thresholds of barium are indicated on the left-hand side.

$$\beta_{1/2}=\frac{2|S_p(0)|^2-3|S_p(1)|^2}{|S_p(0)|^2+3|S_p(1)|^2}\ , \quad (5)$$

$$\beta_{3/2}=\frac{4|S_f(2)|^2+|S_p(2)|^2-3\sqrt{6}[S_f(2)S_p(2)^\dagger+S_f(2)^\dagger S_p(2)]-3|S_p(1)|^2}{5[|S_f(2)|^2+|S_p(2)|^2]+3|S_p(1)|^2} \quad (6)$$

$$\beta_{5/2}=\frac{4|S_f(2)|^2+|S_p(2)|^2-3\sqrt{6}[S_f(2)S_p(2)^\dagger+S_f(2)^\dagger S_p(2)]-7|S_f(3)|^2}{5[|S_f(2)|^2+|S_p(2)|^2]+7|S_f(3)|^2} \quad (7)$$

The photoionization amplitudes

$$S_l(j_t)\equiv\langle(J_cs)J_{cs},l|S(j_t)|J_0j_\gamma\rangle$$

are expressed in terms of reduced transition dipole matrix elements. For the special case under consideration ($J_0=0, J=j_\gamma=1, \mathbf{J}_c+\mathbf{s}=\mathbf{J}_{cs}=\mathbf{j}_t$) we obtain

$$S_l(j_t)=2\pi\lambda^{-1}[4\pi\alpha\hbar\omega_3/3(2j_t+1)]^{1/2}(-1)^{j_t+1+l}$$
$$\times\langle(J_cs)J_{cs},l,J-\|D\|J_0\rangle \quad (8)$$

where $\hbar\omega_3$ is the energy of the photon ionizing the $6sns\ ^1S_0$ state and the minus sign indicates the incoming wave normalization.[26,27] The energy-dependent dipole matrix element [Eq. (8)] is evaluated according to the following equation:

$$\langle(J_cs)J_{cs},l,J-\|D\|J_0\rangle$$
$$=i^{-l}\exp(i\sigma_{l,J_c})\sum_\rho\langle(J_cs)J_{cs},l|\rho\rangle\exp(i\pi\tau_\rho)D_\rho\ , \quad (9)$$

where $\sigma_{l,J_c}=\arg\Gamma(l+1-i/k_{J_c})$ is the Coulomb phase of the outgoing electron, characterized by its orbital angular momentum quantum number l, and wave number k_{J_c}, leaving the Ba^+ ion in the final ionic state J_c. In Eq. (9) the sum is taken over all collision eigenchannels ρ. The corresponding wave functions ψ_ρ, eigenphase shifts $\pi\tau_\rho$, and reduced transition matrix elements $D_\rho=\langle\rho,J=1\|D\|J_0\rangle$ were derived from multichannel quantum-defect theory, described in the following paragraph.

The MQDT equation[28–30] which applies to the bound part of the spectrum reads

$$\sum_{\alpha} U_{i\alpha}\sin[\pi(\nu_i+\mu_\alpha)]A_\alpha=0\ , \tag{10}$$

where i denotes a (closed) dissociation channel. The effective quantum number ν_i is related to the corresponding ionization limit I_i by $\nu_i=[\mathcal{R}/(I_i-E)]^{1/2}$. The matrix $U_{i\alpha}$ diagonalizes the reaction matrix K,[31,32]

$$K=U\tan(\pi\mu)U^{\dagger}\ , \tag{11}$$

where the eigenvalue $\tan(\pi\mu_\alpha)$ corresponds to the eigenquantum defect μ_α of the close-coupling channel ψ_α. The wave function ψ can be expressed in terms of all close-coupling channels as

$$\psi=\sum_{\alpha} A_\alpha\psi_\alpha\ . \tag{12}$$

The amplitudes A_α are obtained from Eq. (10). A nontrivial solution of Eq. (10) requires the determinant of the coefficient matrix to vanish, i.e.,

$$\det|U_{i\alpha}\sin[\pi(\nu_i+\mu_\alpha)]|=0\ . \tag{13}$$

In the autoionizing region [Fig. (6)] Eqs. (10) and (13) need to be modified, by replacing ν_i through $-\tau_\rho$ for all open dissociation channels i. The eigenphase shifts $\pi\tau_\rho$ of the collision eigenchannels are obtained by solving the modified Eq. (13) at each energy E. At large distance r, the wave functions $r^{-1}\psi_\rho$ of the collision channels[29] are given (in a.u.) by

$$\begin{aligned}\psi_\rho\rightarrow&\sum_i \Phi_i(2/\pi k_i)^{1/2}\\&\times\sin[k_i r-(\pi l_i)/2+(1/k_i)\\&\times\ln(2k_i r)+\sigma_{l_i,J_c}+\pi\tau_\rho]T_{i\rho}\\&-\sum_i \Phi_i v(\nu_i,l_i,r)(T^b)_{i\rho}\quad(r\rightarrow\infty)\end{aligned} \tag{14}$$

where Φ_i denotes the wave function of the Ba^+ core and includes the angular part and spin of the electron wave function of the i th dissociation channel. In Eq. (14) the first term represents the continuum part of the wave function while the second sum takes into account the contribution of bound dissociation channels. Accordingly, the first and second sum is taken over open and closed dissociation channels, respectively. Because of the exponentially damped Coulomb wave function $v(\nu_i,l_i,r)$ the second term contributes at smaller values of r only. The amplitudes $T_{i\rho}$ and $(T^b)_{i\rho}$ of the open and bound dissociation channels are given by

$$T_{i\rho}=\sum_{\alpha} U_{i\alpha}\cos[\pi(\mu_\alpha-\tau_\rho)]A^\rho_\alpha \tag{15}$$

and

$$(T^b)_{i\rho}=\sum_{\alpha} U_{i\alpha}\cos[\pi(\nu_i+\mu_\alpha)]A^\rho_\alpha\ , \tag{15'}$$

where the coefficients A^ρ_α are normalized in such a way to make $\sum_i T^2_{i\rho}=1$ for each ρ. This corresponds to the continuum normalization of ψ_ρ per unit energy interval. The amplitude $T_{i\rho}$ represents the projection of the collision eigenchannel ρ onto the jj-coupled open dissociation channel i. The projections $\langle(J_c s)J_{cs}=j_t,l|\rho\rangle$ [cf. Eq. (9)] of the collision eigenstates onto open channels with definite transferred angular momentum $\mathbf{j}_t$ are related to the amplitudes $T_{i\rho}$ via the following recoupling transformation:

$$\langle(J_c s)J_{cs},l|\rho\rangle=\sum_i\langle(J_c s)J_{cs},l,J=1|J_c(sl)j,J=1\rangle T_{i\rho} \tag{16}$$

where the sum is taken over all open dissociation channels i. Combining Eqs. (8), (9), and (16) the photoionization amplitudes $S_l(j_t)$ can be expressed, apart from geometrical factors, by the projection $T_{i\rho}$ of the collision eigenchannels ρ onto the dissociation channels i and the reduced dipole matrix elements D_ρ.

For low-lying states of barium direct photoionization of the outer electron and excitation of the bound part of autoionizing resonances have to be considered simultaneously. Since the excitation of the outer electron occurs close to the atomic core, the dipole matrix elements $D_\rho=\sum_\alpha A^\rho_\alpha D_\alpha$ are expressed in terms of the reduced dipole matrix elements D_α describing the excitation of the close-coupling channels ψ_α. Usually the dipole matrix elements D_α are obtained as semiempirical parameters from a MQDT analysis. In our experiment, however, photoionization of $6sns\ ^1S_0$ Rydberg states proceeds almost exclusively via the $6sns\rightarrow 6p_{3/2}ns$ ($6p_{1/2}ns$) isolated core transition.[3] It follows from a hydrogenic model that the cross section for photoionization of a ns Rydberg electron scales with n^{-3}. This is true for photon energies $h\nu$ much larger than the binding energy of the Rydberg state.[33] Using this model, we have estimated the cross section for direct photoionization of the $6s12s\ ^1S_0$ Rydberg state of barium to be about $\sigma\approx 3\times10^{-17}$ cm^2, orders of magnitude lower than the cross section $\sigma\approx 4\times10^{-14}$ cm^2 of the isolated core excitation $6s12s\ ^1S_0\rightarrow[6p_{3/2}12s]_{J=1}$. Hence photoionization of the $6sns\ ^1S_0$ Rydberg state is accomplished by exciting the $i=[6p_j ns]_{J=1}$ character in the wave function of the collision eigenchannel ρ. The corresponding reduced transition matrix element D_ρ is given by

$$D_\rho=\langle i=6p_j ns\ J=1\|D\|6sns\ J=0\rangle(T^b)_{i\rho}\ . \tag{17}$$

Since one (bound) dissociation channel is excited only, all scattering amplitudes $S_l(j_t)$ contain the reduced matrix element $\langle 6p_j ns\ J=1\|D\|6sns\ ^1S_0\rangle$ as a common factor. Hence the asymmetry parameters $\beta_{1/2}$, $\beta_{3/2}$, and $\beta_{5/2}$ [cf. Eqs (5–7)] do not depend on it. The absorption cross section of the $6sns\ ^1S_0$ Rydberg state is given by

$$\sigma_{\rm tot}=(\tfrac{4}{3})\pi^2\alpha\hbar\omega_3\sum_\rho|D_\rho|^2\ , \tag{18}$$

where the photon energy $\hbar\omega_3$ refers to the third laser beam. Neglecting radiative decay and collisional ionization of the autoionizing Rydberg state, $\sigma_{\rm tot}$ represents the total photoionization cross section of the $6sns\ ^1S_0$ Ryd-

berg state. Following Refs. 2, 5, and 34 the reduced matrix element

$$\langle i = 6p_j ns\, J=1 \| D \| 6sns\ ^1S_0 \rangle$$

can be expressed as

$$\langle i = 6p_j ns\, J=1 \| D \| 6sns\ ^1S_0 \rangle = g_j \langle 6p \| D \| 6s \rangle \langle \nu_e s | \nu_g s \rangle \nu_e^{3/2} (2\mathcal{R})^{-1/2} , \quad (19)$$

where $g_j = \sqrt{1/3}$ ($j = \frac{1}{2}$) and $g_j = \sqrt{2/3}$ ($j = \frac{3}{2}$) represent geometrical factors and the overlap integral $\langle \nu_e s | \nu_g s \rangle$ depends on the effective principal quantum numbers ν_e, ν_g of the Rydberg electron in $[6p_j ns]_{J=1}$ and $6sns\ ^1S_0$ states, respectively. The overlap integral in discrete normalized form[5] is given by

$$\langle \nu_e s | \nu_g s \rangle = [2(\nu_e \nu_g)^{1/2}/(\nu_e + \nu_g)] \times \sin[\pi(\nu_e - \nu_g)]/[\pi(\nu_e - \nu_g)] . \quad (20)$$

The partial cross section for photoionization resulting in a particular final ionic state $Ba^+(J_c)$ can be expressed as

$$\sigma(J_c) = (4\pi^2/3)\alpha\hbar\omega_3 \sum_i \left| \sum_\rho D_\rho \exp(i\pi\tau_\rho) T_{i\rho} \right|^2 . \quad (21)$$

In Eq. (21) the first sum is taken over open dissociation channels which correspond to the particular final ionic state under consideration, only.

IV. RESULTS AND DISCUSSION

In this section we discuss asymmetry parameters $\beta_{J_c} = \beta_{J_c}(E)$ derived from experimentally observed angular distributions, which have been measured as a function of total excitation energy E. The transferred angular momentum formalism outlined in the preceding section will be employed to analyze these data. For this purpose we use several MQDT models which will be discussed in detail. Above the $6p\ ^2P_{1/2}$ limit the physical situation is less complicated than below [Fig. 6] because fewer interacting closed channels have to be taken into account. Therefore simpler MQDT models suffice to analyze the angular distribution of electrons emitted from autoionizing Rydberg states situated above the $6p\ ^2P_{1/2}$ limit which will be discussed first.

In Fig. 7 we show asymmetry parameters $\beta_{1/2} = \beta_{1/2}(E)$ measured in the vicinity of several ($n = 13$, 20, 50, and 100) autoionizing $[6p_{3/2}ns]_{J=1}$ Rydberg states. To facilitate direct comparison, the asymmetry parameters have been plotted versus the effective quantum number $\nu_{3/2}$ referring to the $6p\ ^2P_{3/2}$ limit. Starting from the $6sns\ ^1S_0$ Rydberg level, the frequency of the third laser was varied to cover the energy range between the $[6p_{3/2}(n-2)d]_{J=1}$ and $[6p_{3/2}(n-1)d]_{J=1}$ autoionizing states. Close to these autoionizing states, the asymmetry parameter $\beta_{1/2}$ exhibits pronounced resonances, whereas $\beta_{1/2}$ does not depend on $\nu_{3/2}$ in the vinicity of the $[6p_{3/2}ns]_{J=1}$ states. Furthermore, by comparing the different traces shown in Fig. 7 the asymmetry parameter $\beta_{1/2}$ is seen to be independent of the principal quantum number n of the transition $6sns\ ^1S_0 \rightarrow [6p_{3/2}ns]_{J=1}$. Experimental uncertainties in the effective quantum number $\nu_{3/2}$ are mainly responsible for minor differences between the asymmetry parameter $\beta_{1/2}$ ($n = 100$) and those measured at lower principal quantum numbers. Just as $\beta_{1/2}$, the asymmetry parameters $\beta_{3/2}$ and $\beta_{5/2}$ are independent of the principal quantum number of the transition $6sns\ ^1S_0 \rightarrow [6p_{3/2}ns]_{J=1}$. Figures 8(b) and 8(c) illustrate the variation of the asymmetry parameters $\beta_{3/2}$ and $\beta_{5/2}$ in the vicinity of the $[6p_{3/2}50s]_{J=1}$ autoionizing state. No resonant variations in the asymmetry parameters $\beta_{3/2}$ and $\beta_{5/2}$ are found in the vicinity of the $[6p_{3/2}50s]_{J=1}$ state, whereas broad resonances are observed close to the neighboring $[6p_{3/2}48d]_{J=1}$ and $[6p_{3/2}49d]_{J=1}$ states. This behavior is analogous to the variation of the asymmetry parameter $\beta_{1/2}$ discussed above. The asymmetry parameters $\beta_{1/2}$, $\beta_{3/2}$, and $\beta_{5/2}$ measured at the center of the $[6p_{3/2}20s]_{J=1}$ state agree within error limits with the

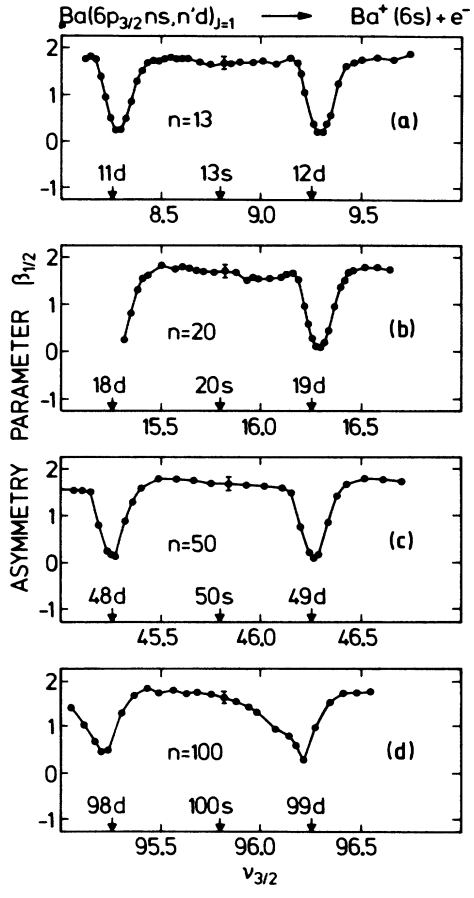

FIG. 7. Experimental asymmetry parameters $\beta_{1/2}$ plotted vs the effective principal quantum number $\nu_{3/2}$, referred to the $6p\ ^2P_{3/2}$ threshold. Starting from the $6sns\ ^1S_0$ ($n = 13$, 20, 50, and 100) Rydberg state, the wavelength of the third ionizing laser [see Fig. 1(c)] was varied to cover the energy range between the $[6p_{3/2}(n-2)d]_{J=1}$ and $[6p_{3/2}(n-1)d]_{J=1}$ autoionizing Rydberg states, marked by arrows. The experimental data (dots) have been connected to guide the eye. Typical error limits are given for each trace.

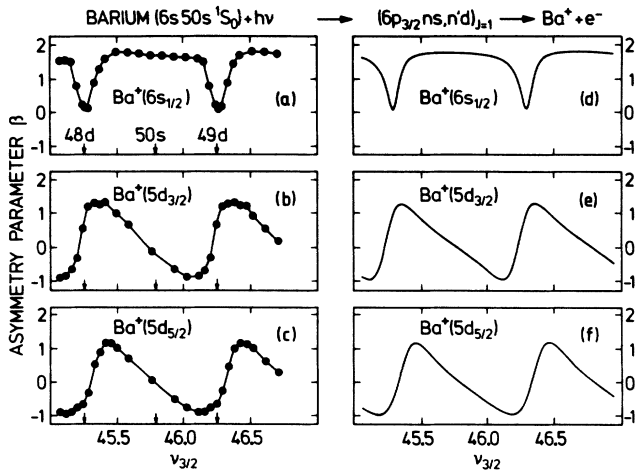

FIG. 8. Comparison of (a)–(c) experimental and (d)–(f) theoretical asymmetry parameters $\beta_{1/2}$, $\beta_{3/2}$, and $\beta_{5/2}$, corresponding to the isolated core excitation $6s \rightarrow 6p_{3/2}$ of the $6s50s\ ^1S_0$ Rydberg state. The positions of the $[6p_{3/2}48d,49d]_{J=1}$ and $[6p_{3/2}50s]_{J=1}$ autoionizing Rydberg states are indicated. Experimental error limits approximately correspond to the size of the dots. The solid curves illustrated in (d)–(f) have been calculated using the MQDT parameters listed in Table I(a)–I(c).

results reported by Kachru *et al.*[9]

These results can be explained qualitatively in the following way. Compared to the excitation of the bound part of the $[6p_{3/2}ns]_{J=1}$ autoionizing state and subsequent decay into the various continua, the direct photoionization of the Rydberg electron of the $6sns\ ^1S_0$ state can be neglected, as was mentioned above. Therefore, above the $6p\ ^2P_{1/2}$ threshold the asymmetry parmeters $\beta_{1/2}$, $\beta_{3/2}$, and $\beta_{5/2}$ are expected to be independent of the excitation energy as long as configuration interactions of the $[6p_{3/2}ns]_{J=1}$ series with other autoionizing Rydberg series can be neglected. For example, in the absence of configuration interactions the relative amplitudes of the outgoing $6s\epsilon p_{1/2}$ and $6s\epsilon p_{3/2}$ waves are independent of the excitation energy, whereas the absorption cross section resonantly varies with energy. Since the asymmetry parameter $\beta_{1/2}$ measures the relative amplitudes of the outgoing $\epsilon p_{1/2}$ and $\epsilon p_{3/2}$ waves, the asymmetry parameter is expected to be constant. The experimentally observed resonant variation of $\beta_{1/2}$ in the vicinity of the $[6p_{3/2}(n-2)d]_{J=1}$ and $[6p_{3/2}(n-1)d]_{J=1}$ autoionizing states is caused by the configuration interaction between the $[6p_{3/2}n'd]_{J=1}$ and $[6p_{3/2}ns]_{J=1}$ autoionizing Rydberg series. This configuration interaction allows the $[6p_{3/2}(n-1)d]_{J=1}$ and $[6p_{3/2}(n-2)d]_{J=1}$ states to be excited from the $6sns\ ^1S_0$ Rydberg state. It should be noted that the $^1S_0$ Rydberg states under consideration are of pure $6sns$ configuration[35–37] and hence the $6p_{3/2}ns$ character can be excited only. Since the coupling of the $[6p_{3/2}n'd]_{J=1}$ series to the continuum channels differs from that of the $[6p_{3/2}ns]_{J=1}$ series, the distribution of the outgoing electrons over the different dissociation channels at large radial distances is modified in the vicinity of the d resonances. It follows from this discussion that no resonances would be observed if the coupling of the $[6p_{3/2}nd]_{J=1}$ series to the $6s\epsilon p_{1/2}$ and $6s\epsilon p_{3/2}$ continua were zero or identical to the coupling of the $[6p_{3/2}ns]_{J=1}$ states to these open channels. Furthermore, if the $[6p_{3/2}nd]_{J=1}$ character were excited by an isolated core transition from a suitably chosen intermediate Rydberg state, the resonance in $\beta_{1/2}$ would occur in the vicinity of the $[6p_{3/2}ns]_{J=1}$ states. The same arguments can be put forward to explain the resonances in the asymmetry parameters $\beta_{3/2}$ and $\beta_{5/2}$ shown in Figs. 8(b) and 8(c). Also, the independence of the resonances $\beta_{1/2}$ on the principal quantum number n of the transition $6sns\ ^1S_0 \rightarrow [6p_{3/2}ns]_{J=1}$ (see Fig. 7) is easily explained. There are no perturbing states between the $6p\ ^2P_{1/2}$ and $6p\ ^2P_{3/2}$ limits of barium, which belong to autoionizing $J=1$ Rydberg series converging towards higher thresholds.[38] Consistent with the isolated core excitation model, direct photoionization of the Rydberg electron can be neglected and hence identical $\beta_{1/2}$ resonances are to be expected for different $6sns\ ^1S_0 \rightarrow [6p_{3/2}ns]_{J=1}$ transitions.

For a quantitative analysis of the angular distributions measured above the $6p\ ^2P_{1/2}$ threshold we have used suitably chosen MQDT models. It follows from Fig. 6 that three bound ($6p_{3/2}ns$, $nd_{3/2}$, and $nd_{5/2}$) and ten open channels are needed for a complete multichannel quantum-defect analysis. Such an analysis allowed a simultaneous description of the angular distributions $\beta_{1/2}$, $\beta_{3/2}$, and $\beta_{5/2}$ as well as of other observables, e.g. absorption cross sections, branching ratios, and spin polarization parameters. However, because of the limited experimental data available we decided to use a separate reduced model for each final ionic state. This is accomplished by introducing composite continuum channels which represent all continuum channels except those belonging to the final ionic state under consideration. For example, the composite continuum channel in the MQDT model used to calculate $\beta_{1/2}$ is comprised of all continua (Fig. 6) except the $6s\epsilon p_{1/2}$ and $6s\epsilon p_{3/2}$ channels. From the discussion given in the preceding paragraph it follows that at least two bound and two open channels are needed to describe resonances in the asymmetry parameter β. We have chosen the $[6p_{3/2}ns]_{J=1}$ and $[6p_{3/2}nd]_{J=1}$ series as closed channels in each case. Since previous attempts to resolve $[6p_{3/2}nd_{3/2}]_{J=1}$ and $[6p_{3/2}nd_{5/2}]_{J=1}$ autoionizing resonances were unsuccessful[10] and hence their individual quantum defects and linewidths are not known, we do not distinguish between these fine-structure components. Hence, the MQDT model used to calculate the asymmetry parameter $\beta_{1/2}$ consists of the five dissociation channels listed in Table I(a). For a calculation of the asymmetry parameters $\beta_{3/2}$ and $\beta_{5/2}$ an additional reduction in the number of open channels is necessary. There are three open channels associated with the $Ba^+\ ^2D_{3/2}$ ($5d_{3/2}\epsilon p_{1/2}$, $\epsilon p_{3/2}$, $\epsilon f_{5/2}$) and $Ba^+\ ^2D_{5/2}$ ($5d_{5/2}\epsilon p_{3/2}$, $\epsilon f_{5/2}$, $\epsilon f_{7/2}$) final ionic states. However, apart from the composite continuum channel, we have chosen the channels $5d\epsilon p$ and $5d\epsilon f$ as continua available to the outgoing electron, neglecting its

spin. The experimental data shown in Fig. 8(b) and Fig. 8(c) support this approximation. As can be seen, the variation of the asymmetry parameters $\beta_{3/2}$ and $\beta_{5/2}$ with energy is nearly identical apart from a slight displacement along the $\nu_{3/2}$ axis, suggesting that the electron spin does not play a dominant role. This approximation is closely related to the Cooper-Zare model[39] and amounts to a total neglect of parity unfavored contributions. Table I(b) and I(c) specify the five dissociation channels of

TABLE I. Dissociation channels and MQDT parameters used to calculate asymmetry parameters (a) $\beta(^2S_{1/2})$, (b) $\beta(^2D_{3/2})$, and (c) $\beta(^2D_{5/2})$ for electrons emitted after isolated core excitation ($6s \rightarrow 6p_{3/2}$) of $6sns\ ^1S_0$ Rydberg states ($n \geq 13$). The acronym CCC denotes the corresponding composite continuum channel.

i,j,α	1	2	3	4	5
		(a) $\beta(^2S_{1/2})$			
$\|i\rangle$	$6s\epsilon p_{3/2}$	$6s\epsilon p_{1/2}$	CCC	$6p_{3/2}nd$	$6p_{3/2}ns$
K_{ij}	−0.73	0.0	0.0	0.24	0.16
		−0.73	0.0	−0.09	−0.22
			0.0	0.9	0.45
				−0.86	0.48
					0.8
$U_{i\alpha}$	0.25	−0.09	0.96	0.01	0.1
	−0.08	0.98	0.13	−0.13	−0.09
	0.49	0.02	−0.17	−0.7	0.5
	−0.83	−0.1	0.18	−0.35	0.38
	0.05	0.17	−0.09	0.61	0.77
μ_α	0.69	0.79	0.81	0.02	0.3
		(b) $\beta(^2D_{3/2})$			
$\|i\rangle$	$5d_{3/2}\epsilon p$	$5d_{3/2}\epsilon f$	CCC	$6p_{3/2}nd$	$6p_{3/2}ns$
K_{ij}	−1.46	0.0	0.0	0.0	0.4
		0.56	0.0	−0.33	0.07
			0.0	−0.55	0.85
				−0.86	0.48
					0.8
$U_{i\alpha}$	−0.75	0.65	0.1	0.02	0.12
	−0.08	−0.12	0.28	−0.95	0.05
	−0.33	−0.36	−0.7	−0.1	0.5
	−0.47	−0.64	0.54	0.28	0.05
	0.33	0.17	0.35	0.1	0.85
μ_α	0.67	0.7	0.0	0.18	0.3
		(c) $\beta(^2D_{5/2})$			
$\|i\rangle$	$5d_{5/2}\epsilon p$	$5d_{5/2}\epsilon f$	CCC	$6p_{3/2}nd$	$6p_{3/2}ns$
K_{ij}	−1.01	0.0	0.0	0.42	0.43
		0.11	0.0	−0.53	0.14
			0.0	−0.31	0.8
				−0.86	0.48
					0.8
$U_{i\alpha}$	−0.5	−0.79	0.28	−0.16	−0.18
	0.27	−0.16	0.47	0.83	−0.03
	0.24	−0.37	−0.73	0.25	−0.46
	0.77	−0.25	0.31	−0.48	−0.14
	−0.17	0.4	0.26	−0.05	−0.86
μ_α	0.69	0.74	0.95	0.12	0.3

the MQDT models used to calculate the asymmetry parameters $\beta_{3/2}$ and $\beta_{5/2}$. The three MQDT models discussed above required the determination of a (symmetric) 5×5 K matrix. According to Eq. (11) diagonalization of the K matrix yields eigenquantum defects and the $U_{i\alpha}$ matrix. Since the bound channels ($i=4,5$) are the same in all three models, the matrix elements K_{44}, K_{45}, and K_{55} were required to be essentially the same in each case. Also, off-diagonal elements between open channels were assumed to be zero ($K_{12}=K_{13}=K_{23}=0$). Experimental evidence for a direct mixing between the autoionizing Rydberg series $[6p_{3/2}nd]_{J=1}$ and $[6p_{3/2}ns]_{J=1}$ was reported recently.[10,14] This mixing was taken into account explicitly by assuming the matrix element K_{45} to be nonzero. The K-matrix elements were determined from our experimental data, complemented by quantum defects, branching ratios, and linewidths, within a least-squares fit procedure. Eigenquantum defects were taken from Armstrong, Wynne, and Esherick,[40] who analyzed the corresponding bound Rydberg series within a MQDT model. The linewidth of the $[6p_{3/2}ns]_{J=1}$ autoionizing Rydberg states was reported to be $\Gamma_s=0.2\nu_{3/2}^{-3}$ (a.u.).[9] The linewidth of the $[6p_{3/2}nd]_{J=1}$ states was estimated to be $\Gamma_d=0.24\nu_{3/2}^{-3}$ (a.u.).[10,14] At the energy of the $[6p_{3/2}ns]_{J=1}$ states the branching ratios for the final ionic states under consideration were inferred from the experimental data of Kachru *et al.*[9] As can be seen from Fig. 8, good agreement between experimental and calculated asymmetry parameters was achieved. In addition, calculated eigenquantum defects essentially agree with those of Ref. 40. Furthermore, calculated linewidths and branching ratios are in reasonable agreement with experimental values. Using the matrices listed in Tables I(a)–I(c), we have calculated the $[6p_{3/2}ns]_{J=1}$ and $[6p_{3/2}nd]_{J=1}$ character according to

$$Z_s^2=\sum_{\rho=1}^{3}(T^b)_{5\rho}^2\ ,\qquad Z_d^2=\sum_{\rho=1}^{3}(T^b)_{4\rho}^2\ . \tag{22}$$

The calculated characters Z_s^2 and Z_d^2 are in essential agreement with the densities illustrated in Fig. 12 of Ref. 10. However, since our experimental data do not allow us to distinguish between a direct coupling of these autoionizing series or an indirect coupling via the continua, the value $K_{45}=0.48$ carries a considerable amount of uncertainty.

Before concluding the discussion of the asymmetry parameters above the $6p\ ^2P_{1/2}$ threshold we want to point out a problem frequently encountered with complicated MQDT analyses. Apart from trivial ambiguities in the sign of some K-matrix elements, it is not possible to uniquely determine the K-matrix elements despite the assumptions made above to reduce the number of MQDT parameters. For example, apart from the K matrix given in Table I(a), there is another K matrix which equally well describes all experimental data available. These two matrices differ in the ratios K_{15}/K_{25} and K_{14}/K_{24}. Using these two matrices we predict different angular distri-

butions $\beta_{1/2}$ if the $[6p_{3/2}nd]_{J=1}$ character were excited only. The autoionizing Rydberg states $[5d_{3/2}nd_{3/2}]_{J=0}$ ($n=26,27,60,61$) recently reported to be effectively bound[41] may serve as suitable intermediate states in such an experiment.

The remaining part of this section is devoted to the analysis of the angular distribution of electrons emitted from $[6p_{1/2}ns]_{J=1}$ and $[6p_{1/2}nd_{3/2}]_{J=1}$ autoionizing states with principal quantum numbers ranging between

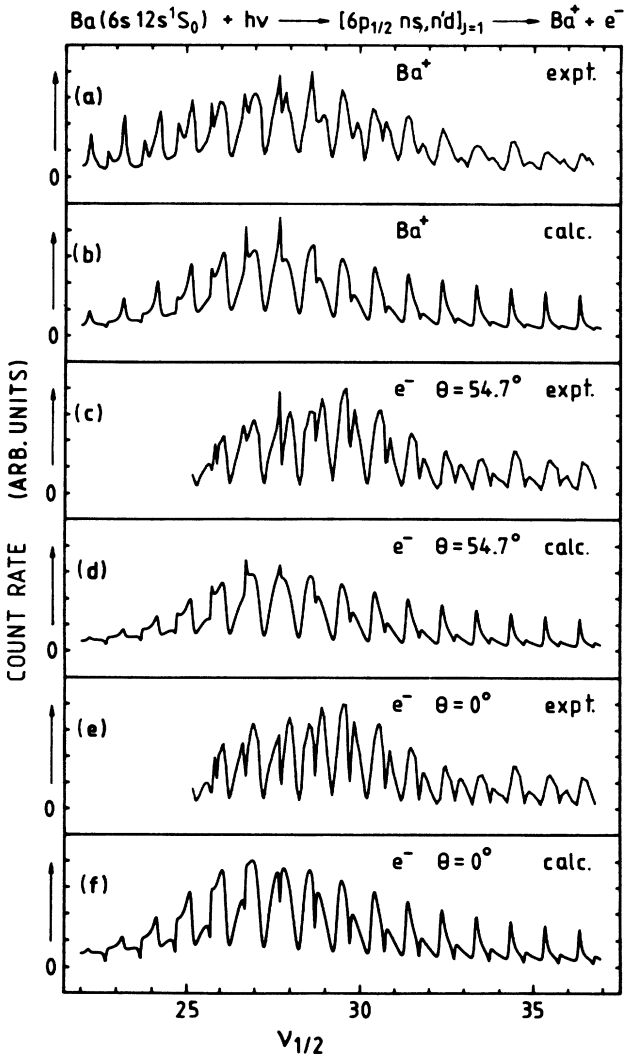

FIG. 9. (a) and (b) are experimental and calculated total ion yields, (c) and (d) are partial ion yields for decays to the Ba^+ ground state, and (e) and (f) are electron yields at $\theta=0°$ corresponding to the $Ba^+ {}^2S_{1/2}$ final ionic state following photoionization of the $6s12s\ {}^1S_0$ Rydberg state through isolated core excitation ($6s\rightarrow 6p_{3/2}$). Data have been plotted vs the effective quantum number $\nu_{1/2}$ related to the $6p\ {}^2P_{1/2}$ threshold. The central portion of trace 9(a) and 9(e) corresponds to the data shown in Fig. 5(c) and Fig. 5(b), respectively. The data shown in (c) were derived from electron yields (e) and experimental asymmetry parameters [Fig. 11(a)]. The theoretical results were obtained within the same MQDT analyses used to calculate the asymmetry parameters shown in Figs. 11(b) and 12(d).

$n=22$ and 50. We have complemented these data by measuring total $\sigma_{\rm tot}=\sigma_{\rm tot}(E)$ and partial $\sigma(J_c)=\sigma(J_c,E)$ photoionization cross sections as well as branching ratios. As can be seen from Fig. 6 the $[6p_{3/2}12s]_{J=1}$ autoionizing state, located just below the $6p\ {}^2P_{1/2}$ ionization limit, is nearly degenerate with a large number of these Rydberg states. Configuration interaction results in a complicated energy dependence of partial and total photoionization cross sections, branching ratios, as well as asymmetry parameters. Figure 9 illustrates experimental total ion yields [Fig. 9(a)], partial ion yields for decays to the $Ba^+\ 6s\ {}^2S_{1/2}$ final ionic state [Fig. 9(c)] and partial photoelectron yields [Fig. 9(e)]. The trace shown in Fig. 9(c) was derived from the experimental spectrum taken at $\theta=0°$ and corrected for the anisotropy of the electron emission using measured asymmetry parameters $\beta_{1/2}$. From electron spectra taken at fixed total excitation energies [see, for example, Fig. 4(a)] we have deduced branching ratios for decays to the final ionic states $Ba^+\ 6s\ {}^2S_{1/2}$, $5d\ {}^2D_{3/2}$, and $5d\ {}^2D_{5/2}$, using experimental asymmetry parameters. For this purpose we have assumed our experimental setup to have the same detection efficiency for electrons leaving the Ba^+ ion in the ${}^2D_{3/2,5/2}$ and ${}^2S_{1/2}$ states. The branching ratios $R_{J_c}=\sigma(J_c)/\sum_k\sigma(k)$

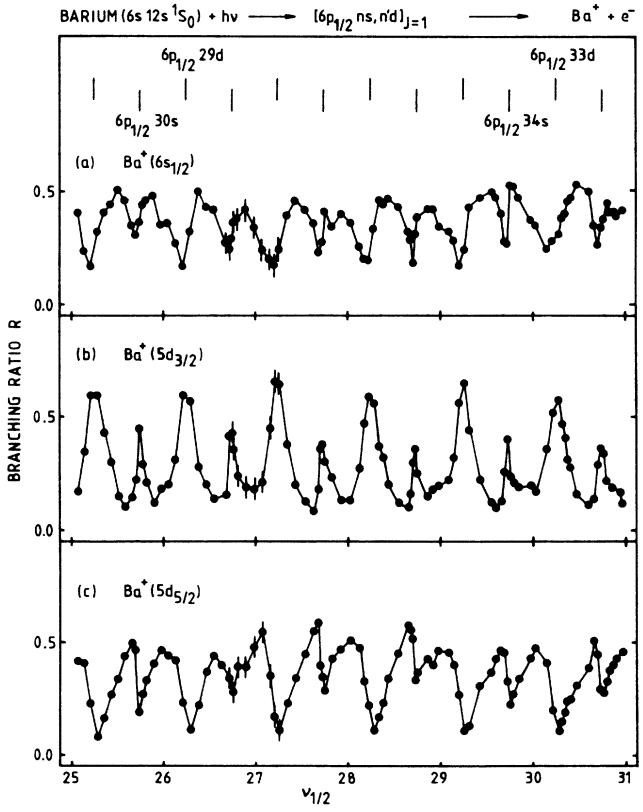

FIG. 10. Experimental branching ratios (a) $R_{1/2}$, (b) $R_{3/2}$, and (c) $R_{5/2}$ following photoionization of the $6s12s\ {}^1S_0$ Rydberg state by isolated core excitation $6s\rightarrow 6p_{3/2}$. The position of the autoionizing Rydberg states are marked in the upper part of this figure. The same energy range centered at the $[6p_{3/2}12s]_{J=1}$ perturber is covered as in Fig. 5. Typical experimental uncertainties are given in each trace at $\nu_{1/2}\approx 27$.

($k=1/2,3/2,5/2$) have been plotted versus the effective principal quantum number $\nu_{1/2}$ in Fig. 10, covering nearly the same energy range as Fig. 5. Asymmetry parameters $\beta_{1/2}$, $\beta_{3/2}$, and $\beta_{5/2}$ derived from experiment and plotted versus $\nu_{1/2}$ are illustrated in Fig. 11. The asymmetry parameters correspond to the isolated core transition $6s12s\ ^1S_0 \rightarrow [6p_{3/2}12s]_{J=1}$ and to the final ionic states $6s\ ^2S_{1/2}$, $5d\ ^2D_{3/2}$, and $5d\ ^2D_{5/2}$, respectively. Besides the data shown in Fig. 11, we have measured asymmetry parameters $\beta_{1/2}$, $\beta_{3/2}$, and $\beta_{5/2}$ corresponding to the isolated core transition $6s24s\ ^1S_0 \rightarrow [6p_{1/2}24s]_{J=1}$. These data were obtained within a limited energy range ($19.4 \leq \nu_{1/2} \leq 20.4$) only. For each final ionic state an appropriately chosen MQDT model was used to calculate total and partial ion yields as well as asymmetry parameters as a function of excitation energy. The experimental data shown in Figs. 9, 11, and 12 are compared with theoretical results.

The MQDT models used to analyze our experimental data above and below the $6p\ ^2P_{1/2}$ threshold are essentially the same for each final ionic state. However, whereas the open channels $6p_{1/2}\epsilon s$ and $6p_{1/2}\epsilon d_{3/2}$ were included in the composite continuum channel, below the $6p\ ^2P_{1/2}$ limit the corresponding closed channels $6p_{1/2}ns$ and $6p_{1/2}nd_{3/2}$ have to be taken into account explicitly in order to analyze the data shown in Figs. 9, 11, and 12. In Tables II(a)–II(c) we list the seven dissociation channels, i.e., three open and four closed ones, for each of the MQDT models together with the K and $U_{i\alpha}$ matrices obtained from least-squares fits. As can be seen from Table II, the open channels $5d_{3/2}\epsilon p_{1/2}$ and $5d_{3/2}\epsilon p_{3/2}$ as well as $5d_{5/2}\epsilon f_{5/2}$ and $5d_{5/2}\epsilon f_{7/2}$ are represented by open channels $5d\epsilon p$ and $5d\epsilon f$, respectively, ignoring the spin of the outgoing electron. It should be noted that the same approximation was made to analyze our data above the $6p\ ^2P_{1/2}$ limit. For each final ionic state asymmetry parameters (cf. Figs. 11 and 12) and total ion yields [cf. Fig. 9(a)] were included in the fit. For the $6s\ ^2S_{1/2}$ final ionic state, however, these data were complemented by the photoelectron yields at $\theta=54.7°$. The same approximations were made and analogous constraints imposed in the fitting procedure as described for the analysis above the $6p\ ^2P_{1/2}$ limit. Off-diagonal elements between open channels were arbitrarily set equal to zero. Furthermore, no direct coupling was considered between the $[6p_{3/2}10d]_{J=1}$ autoionizing state and the Rydberg series $[6p_{1/2}ns]_{J=1}$ and $[6p_{1/2}nd_{3/2}]_{J=1}$. The K-matrix elements between corresponding closed channels were taken to be essentially the same for the three MQDT models (cf. Table II), differing in their open channels only. For a comparison of experimental and theoretical results, calculated and measured total ion yields and electron yields were normalized to the same area. As can be seen from

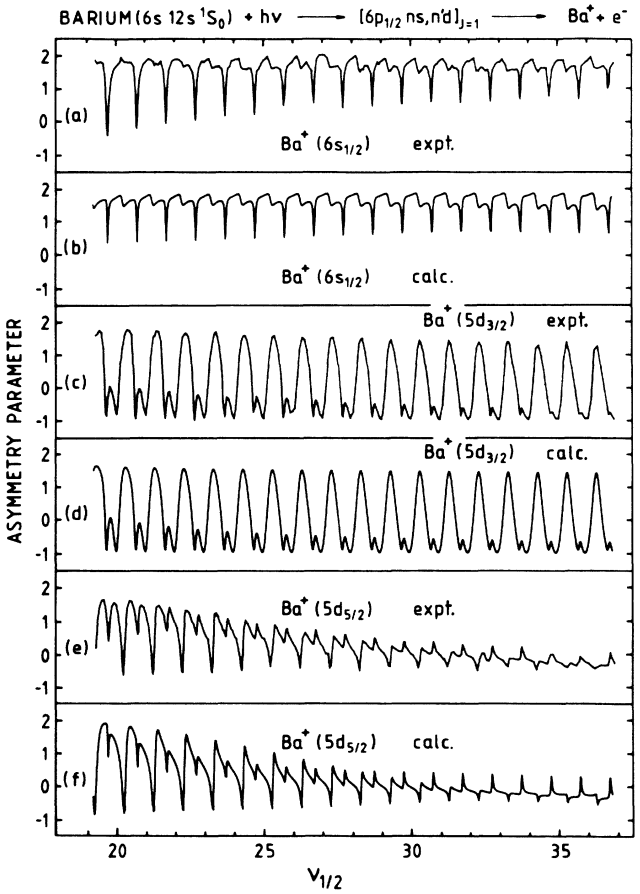

FIG. 11. Experimental and theoretical asymmetry parameters within the contour of the $[6p_{3/2}12s]_{J=1}$ autoionizing resonance, excited from the $6s12s\ ^1S_0$ Rydberg state by isolated core excitation. For clarity, individual experimental data points are not shown but have been connected by straight lines to facilitate comparison with theoretical results. The center portion of trace (a) corresponds to Fig. 5(a). The theoretical results were obtained from MQDT analyses using the parameters given in Table II(a)–II(c).

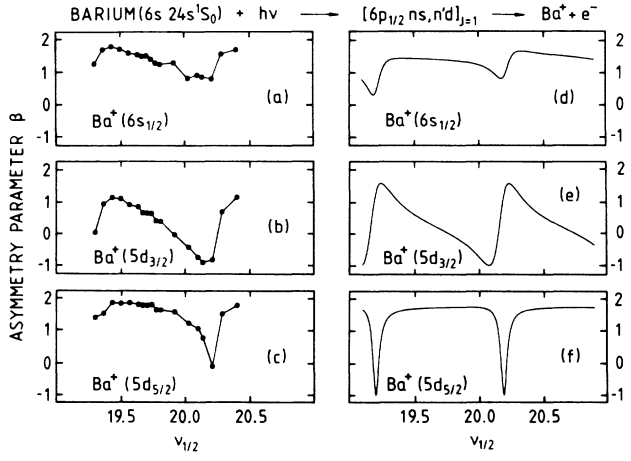

FIG. 12. Comparison of (a)–(c) experimental and (d)–(f) theoretical asymmetry parameters corresponding to the photoionization of the $6s24s\ ^1S_0$ Rydberg state through isolated core excitation ($6s \rightarrow 6p_{1/2}$). The asymmetry parameters should be compared with the leftmost part of Fig. 11. The calculated curves [(d)–(f)] were obtained within the same MQDT analyses yielding the theoretical results shown in Figs. 11(b), 11(d), and 11(f), respectively.

TABLE II. Dissociation channels and MQDT parameters used to calculate asymmetry parameters (a) $\beta(^2S_{1/2})$, (b) $\beta(^2D_{3/2})$, and (c) $\beta(^2D_{5/2})$ for electrons emitted after isolated core excitation ($6s \rightarrow 6p_{3/2}$) of the $6s12s\ ^1S_0$ Ba Rydberg state. The acronym CCC denotes the corresponding composite continuum channel.

i,j,α	1	2	3	4	5	6	7
				(a) $\beta(^2S_{1/2})$			
$\|i\rangle$	$6s\epsilon p_{3/2}$	$6s\epsilon p_{1/2}$	CCC	$6p_{1/2}nd_{3/2}$	$6p_{1/2}ns$	$6p_{3/2}nd$	$6p_{3/2}ns$
K_{ij}	−0.73	0.0	0.0	0.1	−0.49	−0.64	0.48
		−0.73	0.0	0.15	0.11	0.71	−0.7
			0.0	0.53	0.36	0.8	−0.13
				−0.75	−0.23	0.0	0.4
					1.16	0.0	0.2
						−0.86	0.48
							0.7
$U_{i\alpha}$	−0.37	−0.52	−0.52	−0.45	0.05	0.22	0.25
	0.45	−0.09	−0.72	0.33	−0.25	−0.31	−0.09
	0.30	−0.27	0.26	−0.49	−0.65	0.01	−0.33
	−0.22	0.78	−0.32	−0.3	−0.34	0.18	0.0
	−0.13	0.02	−0.18	−0.14	0.41	0.02	−0.88
	−0.64	−0.18	0.04	0.52	−0.49	0.04	−0.22
	0.31	−0.05	−0.05	0.27	−0.01	0.91	−0.07
μ_α	0.63	0.74	0.8	0.89	0.18	0.27	0.31
				(b) $\beta(^2D_{3/2})$			
$\|i\rangle$	$5d_{3/2}\epsilon p$	$5d_{3/2}\epsilon f$	CCC	$6p_{1/2}nd_{3/2}$	$6p_{1/2}ns$	$6p_{3/2}nd$	$6p_{3/2}ns$
K_{ij}	−1.46	0.0	0.0	−0.6	0.07	0.0	0.4
		0.56	0.0	−0.52	−0.5	−0.33	0.07
			0.0	−0.07	−0.46	−0.2	0.6
				−0.86	−0.15	0.0	0.4
					1.69	0.0	0.2
						−0.86	0.48
							0.8
$U_{i\alpha}$	−0.75	−0.38	0.51	−0.01	−0.14	0.1	−0.02
	−0.15	0.21	−0.26	0.15	−0.85	−0.08	0.34
	−0.12	0.31	−0.03	−0.83	0.0	0.4	0.2
	−0.55	0.04	−0.72	0.19	0.34	0.15	−0.02
	−0.06	0.12	−0.12	−0.18	−0.32	−0.04	−0.91
	−0.16	0.8	0.37	0.37	0.14	0.17	−0.07
	0.25	−0.24	−0.02	0.28	−0.16	0.88	−0.08
μ_α	0.65	0.73	0.82	0.94	0.18	0.29	0.35
				(c) $\beta(^2D_{5/2})$			
$\|i\rangle$	$5d_{5/2}\epsilon p$	$5d_{5/2}\epsilon f$	CCC	$6p_{1/2}nd_{3/2}$	$6p_{1/2}ns$	$6p_{3/2}nd$	$6p_{3/2}ns$
K_{ij}	−1.42	0.0	0.0	0.46	−0.24	0.49	0.19
		0.19	0.0	0.02	−0.28	−0.27	0.1
			0.0	0.01	−0.13	0.36	0.49
				−0.7	−0.12	0.0	0.4
					1.1	0.0	0.2
						−0.86	0.5
							0.74
$U_{i\alpha}$	−0.81	0.31	0.4	0.2	0.08	−0.16	0.07
	0.05	0.22	0.14	−0.19	−0.91	−0.23	−0.12
	−0.08	−0.23	0.23	−0.83	0.18	−0.29	0.29
	0.33	−0.42	0.72	0.38	−0.02	−0.17	0.13
	−0.05	0.04	0.19	−0.1	−0.21	0.8	0.52
	0.46	0.78	0.18	−0.02	0.25	−0.15	0.25
	−0.06	−0.12	−0.43	0.28	−0.16	−0.38	0.74
μ_α	0.66	0.76	0.8	0.94	0.07	0.28	0.29

Figs. 9, 11, and 12, calculated and experimental ion yields, electron yields, and asymmetry parameters agree well and all qualitative features observed experimentally have been reproduced theoretically. In addition, although we did not include measured branching ratios in the fitting procedure, our theoretical results qualitatively account for the modulations observed for $R_{1/2}$ and $R_{3/2}$, whereas discrepancies exist for $R_{5/2}$. Minor quantitative differences are observed between calculated and experimental asymmetry parameters shown in Fig. 12 as well as total and partial ion yields illustrated in Fig. 9. Apart from experimental uncertainties associated with total ion and electron yields, as well as branching ratios these discrepancies probably reflect the limitations of the reduced MQDT models used.

Apart from modulations caused by the rapidly varying channels $6p_{1/2}ns,nd_{3/2}$ the contour of the $[6p_{3/2}12s]_{J=1}$ autoionizing resonance is discernible in all traces of Fig. 9. The total ion yield shown in Fig. 9(a) is in good agreement with previous experimental results,[4,16] which were obtained using three-step pulsed dye laser excitation. As mentioned earlier, the pronounced modulations in the total and partial ion yields and partial electron yield are caused by configuration interaction of $[6p_{1/2}nd_{3/2}]_{J=1}$ Rydberg states with the $[6p_{3/2}12s]_{J=1}$ perturber. The smaller and narrower resonances are associated with $[6p_{1/2}ns]_{J=1}$ levels. As can be seen from Fig. 9(a), a change in the line shapes of the modulations occurs across the contour of the $[6p_{3/2}12s]_{J=1}$ resonance, corresponding to a change in the sign of the Fano q parameter ("q reversal").[18,42] In addition the (normalized) linewidths of the $[6p_{1/2}ns]_{J=1}$ and $[6p_{1/2}nd_{3/2}]_{J=1}$ resonances are seen to increase with increasing effective principal quantum number $\nu_{1/2}$. From Figs. 9(a) and 9(c) it is evident that the modulations exhibited by the total and partial ion yields are very similar. However, the latter one generally shows more pronounced minima. This is consistent with the branching ratio $R_{1/2}$ illustrated in Fig. 10(a). Likewise, the difference between the partial ion yield and the electron spectrum shown in Figs. 9(c) and 9(e), respectively, can be accounted for considering the resonant variations in the asymmetry parameter $\beta_{1/2}$. The line shapes of the resonances observed in the total ion yield, associated with $[6p_{1/2}nd_{3/2}]_{J=1}$ and $[6p_{1/2}ns]_{J=1}$ Rydberg states [Figs. 9(a) and 9(b)], depend on the matrix elements K_{i4} and K_{i5} ($i=1-3$), respectively, as well as on the elements K_{47} and K_{57}. It should be noted that resonances would be observed even when $K_{i4}=K_{i5}=0$ for $i=1-3$.

Figure 10(a)–10(c) illustrate branching ratios $R_{1/2}$, $R_{3/2}$, and $R_{5/2}$ measured in the vicinity of the $[6p_{3/2}12s]_{J=1}$ perturbing resonance. Pronounced modulations are observed in each case, corresponding to window-like resonances for $R_{1/2}$ and $R_{5/2}$. Similar to the structure observed for ion and electron yields, narrow resonances are associated with $[6p_{1/2}ns]_{J=1}$ states, while $[6p_{1/2}nd_{3/2}]_{J=1}$ states cause broad modulations. For example, at the center of the $[6p_{1/2}nd_{3/2}]_{J=1}$ resonance, the decay occurs predominantly to the $5d\ ^2D_{3/2}$ final ionic state, whereas at $[6p_{1/2}ns]_{J=1}$ states all final ionic states are observed with about equal probability. The branching ratios measured halfway between $[6p_{1/2}ns]_{J=1}$ and $[6p_{1/2}nd_{3/2}]_{J=1}$ states are consistent with branching ratios reported for $[6p_{3/2}ns]_{J=1}$ states ($n \geq 13$) above the $6p\ ^2P_{1/2}$ threshold[9] and reflect the contribution of the $[6p_{3/2}12s]_{J=1}$ perturber. The modulations exhibited by the branching ratios show that the $[6p_{1/2}ns,nd]_{J=1}$ states and the $[6p_{3/2}12s]_{J=1}$ perturber differ considerably in their coupling to open channels associated with the three final ionic states. Another manifestation of these differences in continuum couplings are the resonances in the asymmetry parameters (Figs. 11 and 12), which will be discussed in the remaining part of this section.

In the following paragraph the asymmetry parameters $\beta_{1/2}$ observed below the $6p\ ^2P_{1/2}$ limit and illustrated in Figs. 11(a) and 11(b) and Figs. 12(a) and 12(d) are compared with those [Figs. 7, 8(a), and 8(d)] obtained above this threshold. As mentioned in Sec. II the asymmetry parameter $\beta_{1/2}$ exhibits pronounced, symmetric resonances in the vicinity of the $[6p_{1/2}ns]_{J=1}$ Rydberg states [Figs. 11(a) and 11(b)]. The $[6p_{1/2}ns]_{J=1}$ states modulate the continuum, causing resonant variations in the amplitudes of the open dissociation channels. This situation is physically similar to the one encountered above the $6p\ ^2P_{1/2}$ threshold, where a resonance in $\beta_{1/2}$ appears in the vicinity of $[6p_{3/2}nd]_{J=1}$ Rydberg states [Figs. 7, 8(a), and 8(d)]. In both cases resonances occur in the vicinity of autoionizing Rydberg states, coupled to the $[6p_{3/2}ns]_{J=1}$ channel by configuration interaction. These resonances are observed when exciting their $[6p_{3/2}ns]_{J=1}$ character by inducing the $6s \rightarrow 6p_{3/2}$ core transition. Another example is provided by Figs. 12(a) and 12(d). The channels $[6p_{1/2}ns]_{J=1}$ and $[6p_{1/2}nd_{3/2}]_{J=1}$ are mixed by configuration interaction. When exciting the $[6p_{1/2}24s]_{J=1}$ character of the $[6p_{1/2}23d_{3/2}]_{J=1}$ Rydberg state ($\nu_{1/2}=20.3$) by inducing the $6s24s \rightarrow 6p_{1/2}24s$ isolated core transition, a resonance in $\beta_{1/2}$ is observed close to the $[6p_{1/2}23d_{3/2}]_{J=1}$ state. On the contrary, no resonant variation of $\beta_{1/2}$ is detected in the vicinity of the $[6p_{1/2}24s]_{J=1}$ Rydberg state itself ($\nu_{1/2}=19.7$). Because of additional configuration interactions of the $[6p_{1/2}nd_{3/2}]_{J=1}$ and $[6p_{1/2}ns]_{J=1}$ channels with the $[6p_{3/2}10d]_{J=1}$ and $[6p_{3/2}12s]_{J=1}$ perturbers, the line shapes of the resonances in the asymmetry parameter $\beta_{1/2}$ change across the contours of these perturbing states. This is supported by our MQDT analyses and indicated in Fig. 12(d). Similarly, in Figs. 11(a) and 11(b) a slight decrease in the amplitudes of the resonances attributed to the $[6p_{1/2}ns]_{J=1}$ Rydberg states is seen to occur with increasing excitation energy, due to the $[6p_{3/2}10d]_{J=1}$ and $[6p_{3/2}11d]_{J=1}$ perturbing states.

Contrary to the pronounced resonances caused by the $[6p_{1/2}ns]_{J=1}$ states, only small, dispersion-like variations in $\beta_{1/2}$ are found in the vicinity of $[6p_{1/2}nd_{3/2}]_{J=1}$ states [Figs. 11(a) and 11(b)]. Despite the small amplitudes of these resonances the $[6p_{1/2}nd_{3/2}]_{J=1}$ and $[6p_{3/2}12s]_{J=1}$ states considerably differ in their coupling to the open channels, which is also consistent with the rather large widths of the observed modulations. Also, the line shapes of these resonances change across the contour of

the $[6p_{3/2}12s]_{J=1}$ state because of the $[6p_{3/2}10d,11d]_{J=1}$ perturbing states.

The K matrix listed in Table II(a) supports the qualitative discussion given above. The matrix elements K_{i4} (K_{i5}) between the $6p_{1/2}nd_{3/2}$ ($6p_{1/2}ns$) channels and the continuum channels $6s\epsilon p_{3/2}$ ($i=1$) and $6s\epsilon p_{1/2}$ ($i=2$), and the composite continuum channel ($i=3$) are different from the corresponding ones (K_{i7}, $i=1-3$) of the $[6p_{3/2}12s]_{J=1}$ state. This corresponds to a different coupling of the $[6p_{1/2}ns]_{J=1}$ and $[6p_{1/2}nd_{3/2}]_{J=1}$ series to the continua compared to the $[6p_{3/2}12s]_{J=1}$ perturbing state. Contrary to the total ion yield discussed above, no resonances in the asymmetry parameter $\beta_{1/2}$ (and $\beta_{3/2}$ and $\beta_{5/2}$) would be observed if $K_{i4}=K_{i5}=0$ for $i=1-3$. As can be seen from Table II(a), a nonzero matrix element K_{45}, accounting for a direct coupling of the $6p_{1/2}ns$ and $6p_{1/2}nd_{3/2}$ closed channels has been included in our fit procedure. The data shown in Figs. 12(a) and 12(d) suggest a direct coupling between these channels. However, because of the many indirect couplings between these channels, the values obtained for K_{45} carry a large uncertainty reflected by the scatter for K_{45} in the three different MQDT models [Tables II(a)–II(c)].

The variations of the asymmetry parameters $\beta_{3/2}$ and $\beta_{5/2}$ differ substantially across the contour of the $[6p_{3/2}12s]_{J=1}$ perturbing state as can be seen from Figs. 11(c) and 11(d) and Figs. 11(e) and 11(f), respectively. This is in contrast to the situation encountered above the $6p\ ^2P_{1/2}$ threshold, where the energy dependence of $\beta_{3/2}$ and $\beta_{5/2}$ was found to be almost identical (Fig. 8). In Figs. 11(c) and 11(d), the pronounced modulations in the asymmetry parameter $\beta_{3/2}$ are caused by the coupling of the $[6p_{1/2}nd_{3/2}]_{J=1}$ Rydberg series to the $5d\epsilon p$ and $5d\epsilon f$ open channels. Window-like resonances at the right-hand shoulder of these modulations originate from $[6p_{1/2}ns]_{J=1}$ states. The amplitude of these window resonances is seen to decrease with increasing energy. According to Table II(b) the matrix element (K_{15}) between the $6p_{1/2}ns$ and $5d_{3/2}\epsilon p$ channels is negligible compared to the matrix element (K_{25}) between the same closed channel and the $5d_{3/2}\epsilon f$ continua. This is interpreted to represent a stronger coupling of the $[6p_{1/2}ns]_{J=1}$ series to the ϵf compared to the ϵp continuum. However, a coupling of the $6p_{1/2}ns$ and $5d_{3/2}\epsilon f$ channels requires an octupole term in the expansion of the corresponding exchange integrals, whereas a dipole term is needed for the coupling of the $[6p_{1/2}ns]_{J=1}$ Rydberg series to the $5d\epsilon p$ open channel. A considerably larger octupole compared to a dipole expansion term is surprising and may be explained by the total neglect of the spin of the outgoing electron.

The overall decrease in the asymmetry parameter $\beta_{5/2}$, illustrated in Figs. 11(e) and 11(f), parallels the variation of $\beta_{5/2}$ observed above the $6p\ ^2P_{1/2}$ threshold [Figs. 8(c) and 8(f)]. The fast varying channels $6p_{1/2}ns$ and $6p_{1/2}nd_{3/2}$ cause window-like or dispersion-like resonances, which are seen to change with increasing excitation energy. The more pronounced resonances appear in the vicinity of the $[6p_{1/2}nd_{3/2}]_{J=1}$ Rydberg states. As can be seen from Table II(c) the K-matrix element (K_{14}) between the $6p_{1/2}nd_{3/2}$ channel and the $5d_{5/2}\epsilon p$ continuum far outweighs the matrix elements of this closed channel with all other continua. This is taken to represent a predominant coupling of the $[6p_{1/2}nd_{3/2}]_{J=1}$ Rydberg states to the $5d_{5/2}\epsilon p$ continuum. By the same arguments, the $[6p_{1/2}ns]_{J=1}$ Rydberg states experience about the same coupling to the $5d_{5/2}\epsilon p$ and $5d_{5/2}\epsilon f$ continua.

The asymmetry parameters $\beta_{3/2}$ and $\beta_{5/2}$ shown in Figs. 12(b) and 12(e) and Figs. 12(c) and 12(f) correspond to the isolated core excitation $6s24s\ ^1S_0 \rightarrow [6p_{1/2}24s]_{J=1}$. The rapid variation of the asymmetry parameters with energy occurs in the vicinity of the $[6p_{1/2}22d_{3/2},23d_{3/2}]_{J=1}$ ($\nu_{1/2}=19.3,20.3$) states in each case. Again, no resonance is found in the vicinity of the $[6p_{1/2}24s]_{J=1}$ autoionizing state ($\nu_{1/2}=19.7$), consistent with the discussion given above. The shape of the $\beta_{3/2}$ resonance is strikingly similar to that observed for $\beta_{3/2}$ above the $6p\ ^2P_{1/2}$ limit [Figs. 8(b) and 8(e)]. However, our calculations indicate that the shape of the β resonances observed below this limit is strongly dependent on the coupling of the $[6p_{1/2}nd_{3/2}]_{J=1}$ Rydberg states to the $[6p_{3/2}10d]_{J=1}$ and $[6p_{3/2}12s]_{J=1}$ perturbers and therefore is expected to dramatically vary across the contour of these perturbing resonances. Much information could be gained by measuring the angular distribution of emitted electrons following the isolated core excitation $6sns\ ^1S_0 \rightarrow [6p_{1/2}ns]_{J=1}$ across the contour of these perturbing resonances.

V. SUMMARY

We have investigated photoionization of spherically symmetric Ba Rydberg states employing high resolution laser and electron spectroscopy. Photoionization of $6sns\ ^1S_0$ ($n=12$, 13, 20, 50, and 100) Rydberg states was accomplished by isolated core excitation. Besides total and partial ion yields we have measured angular distributions of emitted electrons as function of excitation energy below ($n=12$) and above ($n\geq 13$) the $6p\ ^2P_{1/2}$ threshold. Below this limit branching ratios and asymmetry parameters deduced from our measurements as well as total and partial ion yields show pronounced resonant variations across the contour of the $[6p_{3/2}12s]_{J=1}$ perturbing resonance. These modulations are caused by configuration interactions of $[6p_{1/2}ns,nd_{3/2}]_{J=1}$ and $[6p_{3/2}12s]_{J=1}$ Rydberg states and reflect differences in the continuum couplings of the closed channels involved. The line shapes of the various resonances observed change across the contour of the $[6p_{3/2}12s]_{J=1}$ perturbing resonance due to the presence of neighboring $[6p_{3/2}10d,11d]_{J=1}$ states. Above the $6p\ ^2P_{1/2}$ limit resonances in asymmetry parameters, observed in the vicinity of $[6p_{3/2}nd]_{J=1}$ Rydberg states, originate from configuration interaction between the $6p_{3/2}nd$ and $6p_{3/2}ns$ channels as well as differences in their continuum couplings. Because these Rydberg series are not perturbed any further, the reso-

nances observed are independent of principal quantum number n.

Using restricted MQDT models asymmetry parameters have been calculated as function of excitation energy above and below the $^2P_{1/2}$ threshold. Good to satisfactory agreement with experiment was achieved. However, our experimental results warrant a more complete analysis, in particular a comparison with predictions of eigenchannel R-matrix calculations.

ACKNOWLEDGMENTS

This work was supported by the Deutsche Forschungsgemeinschaft (DFG), Sonderforschungsbereich 161 (Hyperfeinwechselwirkungen) and through the DFG Grant No. Ri 378/1-1. We thank Dr. G. Jönsson for providing experimental expertise. The loan of the ^{130}Te-vapor cell from Professor G. Huber and Dr. J. Eberz is gratefully acknowledged.

*Present address: Physikalisch-Technische Bundesanstalt, Institut Berlin, Abbestrasse 2-12, 1000 Berlin 10, West Germany.

[1]J. Berkowitz, Adv. Chem. Phys. **72**, 1 (1988), and references therein.

[2]W. E. Cooke, T. F. Gallagher, S. A. Edelstein, and R. M. Hill, Phys. Rev. Lett. **40**, 178 (1978).

[3]W. E. Cooke and T. F. Gallagher, Phys. Rev. Lett. **41**, 1648 (1978).

[4]W. E. Cooke and S. A. Bhatti, Phys. Rev. A **26**, 391 (1982).

[5]S. A. Bhatti and W. E. Cooke, Phys. Rev. A **28**, 756 (1983).

[6]W. Sandner, R. Kachru, K. A. Safinya, F. Gounand, W. E. Cooke, and T. F. Gallagher, Phys. Rev. A **27**, 1717 (1983).

[7]F. Gounand, T. F. Gallagher, W. Sandner, K. A. Safinya, and R. Kachru, Phys. Rev. A **27**, 1925 (1983).

[8]N. H. Tran, P. Pillet, R. Kachru, and T. F. Gallagher, Phys. Rev. A **29**, 2640 (1984).

[9]R. Kachru, N. H. Tran, P. Pillet, and T. F. Gallagher, Phys. Rev. A **31**, 218 (1985).

[10]R. Kachru, H. B. van Linden van den Heuvell, and T. F. Gallagher, Phys. Rev. A **31**, 700 (1985).

[11]W. Sandner, U. Eichmann, V. Lange, and M. Völkel, J. Phys. B **19**, 51 (1986).

[12]E. Y. Xu, Y. Zhu, O. C. Mullins, and T. F. Gallagher, Phys. Rev. A **33**, 2401 (1986).

[13]Y. Zhu, E. Y. Xu, and T. F. Gallagher, Phys. Rev. A **36**, 3751 (1987).

[14]L. D. Van Woerkom and W. E. Cooke, Phys. Rev. A **37**, 3326 (1988).

[15]R. R. Jones and T. F. Gallagher, Phys. Rev. A **38**, 2846 (1988).

[16]R. R. Jones and T. F. Gallagher, Phys. Rev. A **39**, 4583 (1989).

[17]V. Lange, U. Eichmann, and W. Sandner, J. Phys. B **22**, L245 (1989).

[18]W. E. Cooke and C. L. Cromer, Phys. Rev. A **32**, 2725 (1985).

[19]C. H. Greene and L. Kim, Phys. Rev. A **36**, 2706 (1987).

[20]L. Kim and C. H. Greene, Phys. Rev. A **36**, 4272 (1987).

[21]M. Aymar and J. M. Lecomte, J. Phys. B **22**, 223 (1989).

[22]J. Cariou and P. Luc, *Atlas du Spectre d'Absorption de la Molecule de Tellure* (1980), available from Laboratoire Aimé-Cotton CNRS, II, 91405 Orsay, France.

[23]H. Rinneberg, J. Neukammer, U. Majewski, and G. Schönhense, Phys. Rev. Lett. **51**, 1546 (1983).

[24]K. Jost, J. Phys. E **12**, 1006 (1979).

[25]J. Neukammer, G. Jönsson, A. König, K. Vietzke, H. Hieronymus, and H. Rinneberg, Phys. Rev. A **38**, 2804 (1988).

[26]U. Fano and D. Dill, Phys. Rev. A **6**, 185 (1972).

[27]D. Dill, Phys. Rev. A **7**, 1976 (1973).

[28]U. Fano, Phys. Rev. A **2**, 353 (1970).

[29]K. T. Lu, Phys. Rev. A **4**, 579 (1971).

[30]C. M. Lee and K. T. Lu, Phys. Rev. A **8**, 1241 (1973).

[31]M. J. Seaton, Proc. Phys. Soc. London **88**, 801 (1966).

[32]M. J. Seaton, Rep. Prog. Phys. **46**, 167 (1983).

[33]H. A. Bethe and E. E. Salpeter, *Quantum Mechanics of One- and Two-Electron Atoms* (Springer-Verlag, Berlin, 1957), p. 299ff.

[34]S. A. Bhatti, C. L. Cromer, and W. E. Cooke, Phys. Rev. A **24**, 161 (1981).

[35]J. Neukammer, E. Matthias, and H. Rinneberg, Phys. Rev. A **25**, 2426 (1982).

[36]W. Hogervorst and E. R. Eliel, Z. Phys. A **310**, 19 (1983).

[37]M. Aymar, P. Camus, M. Dieulin, and C. Morillon, Phys. Rev. A **18**, 2173 (1978).

[38]C. M. Brown and M. L. Ginter, J. Opt. Soc. Am. **68**, 817 (1978).

[39]J. Cooper and R. N. Zare, J. Chem. Phys. **48**, 942 (1968).

[40]J. A. Armstrong, J. J. Wynne, and P. Esherick, J. Opt. Soc. Am. **69**, 211 (1979).

[41]J. Neukammer, H. Rinneberg, G. Jönsson, W. E. Cooke, H. Hieronymus, A. König, K. Vietzke, and H. Spinger-Bolk, Phys. Rev. Lett. **55**, 1979 (1985).

[42]J. P. Connerade, A. M. Lane, and M. A. Baig, J. Phys. B **18**, 3507 (1985).